ACS OMEGA

Open Access

This article is licensed under CC-BY-NC-ND 4.0

http://pubs.acs.org/journal/acsodf

Article

Integrated Optothermal Paperfluidic Platform for Single-Step, Model-Driven CRISPR-Cas12a Diagnostics of *Mycobacterium tuberculosis*

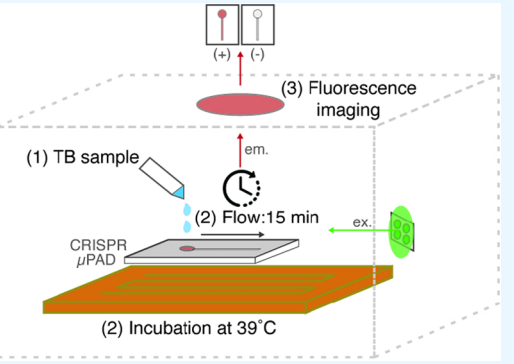
Aujchara Thepbut, Thitipa Rupprom, Lin T. Thant, Hein K. Nyein, Peeraphan Compiro, Pornchai Kaewsapsak, and Pimkhuan Hannanta-anan*

Cite This: *ACS Omega* 2026, 11, 31169−31181

Read Online

ACCESS | Metrics & More | Article Recommendations | Supporting Information

ABSTRACT: CRISPR-Cas12a molecular diagnostics offer high sensitivity and specificity for pathogen detection, yet their translation to point-of-care (POC) settings is often hindered by complex reagent handling, precise thermal requirements, and reliance on bulky laboratory equipment. In this study, we present an integrated opto-thermal paperfluidic platform engineered for the autonomous, single-step CRISPR-Cas12a detection of *Mycobacterium tuberculosis* (MTB). The platform's architecture was optimized by comparing laser and thermal transfer printing, identifying the latter as the superior method for creating robust, leak-proof hydrophobic barriers while preserving the structural integrity of the cellulose substrate. To achieve autonomous operation, we developed a hybrid mathematical model—incorporating boundary resistance and thermal evaporation—to design an "intrinsic timer" that aligns capillary flow front progression with the 15 min CRISPR reaction kinetics. Thermal regulation and signal readout are managed by a custom-engineered, 3D-printed hardware module that provides closed-loop 39 °C incubation and high-contrast fluorescence imaging. By utilizing a red-shifted ROX−quencher reporter probe to overcome paper autofluorescence and sucrose-based lyoprotection for reagent stabilization, the platform achieved a limit of detection of 0.0335 ng/μL with prestored reagents. Our integrated detection system requires only a single sample-loading step and provides results in 15 min, offering a practical, low-cost solution for decentralized tuberculosis surveillance in resource-limited environments.



Downloaded via 58.215.212.98 on June 10, 2026 at 00:44:09 (UTC).
See https://pubs.acs.org/sharingguidelines for options on how to legitimately share published articles.

1. INTRODUCTION

CRISPR-Cas12a molecular diagnostics has emerged as a versatile tool for pathogen detection, offering a compelling alternative to gold-standard methods such as quantitative PCR (qPCR).[1] CRISPR-based platforms achieve sensitivity and specificity comparable to qPCR while remaining significantly more cost-effective and accessible for decentralized testing in resource-limited settings.[2,3] The CRISPR-Cas12a system utilizes a guide RNA (gRNA) to identify specific DNA sequences; upon target recognition, the Cas12a effector protein undergoes conformational activation, triggering its nonspecific trans-cleavage activity. This results in the indiscriminate degradation of surrounding single-stranded DNA (ssDNA) reporter probes, where the cleavage of a fluorophore-quencher (FQ) pair yields a detectable fluorescent signal.[4,5] Consequently, CRISPR-Cas12a-based point-of-care (POC) sensing holds immense potential for the analysis of infectious diseases.

Despite these intrinsic biochemical advantages, current CRISPR diagnostic workflows are not yet optimized for true POC deployment. Standard laboratory formats still require multiple manual reagent-handling steps, stringent thermal regulation (typically 39 °C), and trained personnel to prevent cross-contamination. Furthermore, reliance on bulky heat blocks and benchtop transilluminators or plate readers increases operational costs and limits field accessibility.[6,7] To fully realize the potential of CRISPR diagnostics in low-resource environments, the reaction must be integrated within a self-contained, automated device that operates reliably with minimal user intervention.

Microfluidic technologies offer a robust solution to these challenges by enabling low-volume reagent usage, faster detection kinetics, and the potential for monolithic integration of complex operations.[8] Specifically, microfluidic paper-based analytical devices (μPADs) have emerged as an ideal substrate for POC diagnostics due to several advantages: (i) low-cost fabrication, (ii) ease of handling and disposal, (iii) autonomous fluid transport via capillary action, and (iv) high biocompat-

Received: January 22, 2026
Revised: May 7, 2026
Accepted: May 14, 2026
Published: May 18, 2026



© 2026 The Authors. Published by American Chemical Society

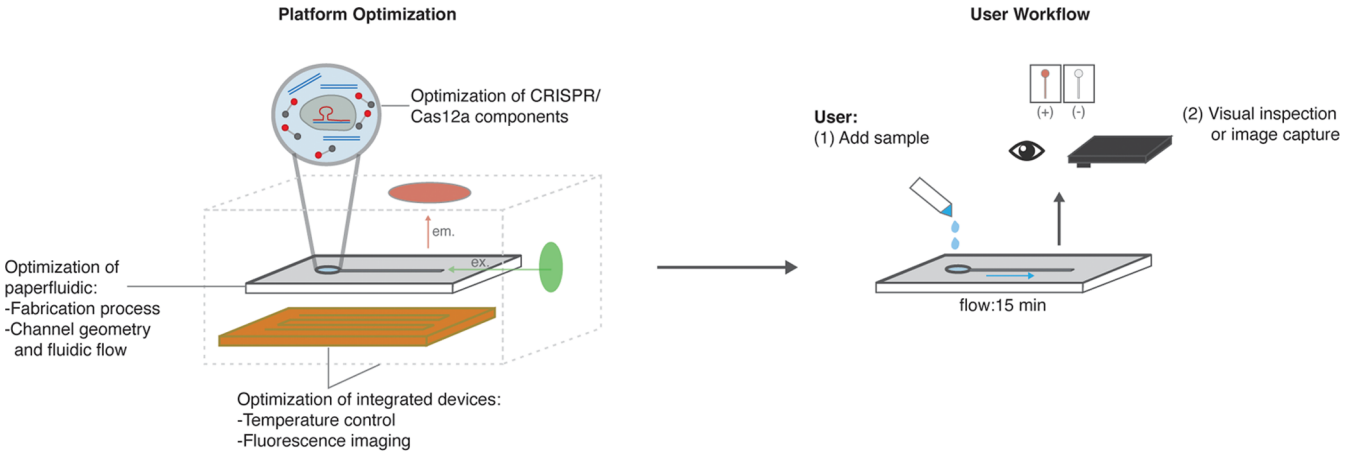


Figure 1. System Overview of the Integrated Opto-thermal Paperfluidic Detection Platform. A three-pronged engineering approach optimizes the workflow for decentralized MTB diagnostics. (Left) Optimization of integrated components: this visual map details the consolidation of key functional modules: (i) the paperfluidic design (optimized fabrication, geometry, and wicking kinetics to act as an intrinsic 15 min timer); (ii) the opto-thermal module (integrated 39 °C temperature control and smartphone-based fluorescence imaging); and (iii) the prestored CRISPR-Cas12a reagents (optimized enzyme, gRNA, and reporter chemistry on paper). (Right) Integrated user workflow: the platform reduces the user interface to two manual steps within a closed-loop environment. Following (1) sample addition to the inlet reservoir, the "intrinsic timer" wicks the sample for 15 min, synchronizing rehydration, mixing, and incubation. (2) At the 15 min mark, the optimized optical path provides clear visual inspection or image capture for objective results. This integrated design consolidated disparate steps (heating, timing, and imaging) into a simplified, robust, and cost-effective device architecture.

ibility.[9] While μPADs are a promising platform for CRISPR-based testing, many reported applications use paper primarily as a static substrate for the final readout of an assay previously performed in a test tube.[10−12]

Recent advancements have attempted to bridge this gap. For instance, Yin et al.[13] developed an autonomous lab-on-paper platform utilizing a 3D-printed reactor and a sucrose valve to automate the transition from amplification to CRISPR detection. Similarly, Sen et al.[14] demonstrated a paper-based LAMP-CRISPR-Cas12a assay for *E. coli* using a custom heating system. However, these systems often rely on complex auxiliary components that increase fabrication difficulty or fail to incorporate rigorous predictive modeling of solution flow and thermal distribution. These omissions hinder the development of a fully integrated, all-in-one paper-based CRISPR diagnostic that is truly user-friendly and reproducible.

In this study, we present a geometry-optimized μPAD platform engineered for the fully integrated CRISPR-based detection of *Mycobacterium tuberculosis* (MTB). To establish a robust foundation for the device, we evaluated laser and thermal transfer printing to identify the superior method for constructing robust hydrophobic barriers. Building upon this fabrication protocol, our system incorporates four key innovations: (i) precise, closed-loop thermal regulation achieved through optimized heat-conducting intermediate materials, (ii) predictive wicking regulation using a hybrid mathematical model of capillary transport, (iii) stable on-chip prestorage of CRISPR reagents via sucrose-based lyoprotection, and (iv) compact fluorescence imaging module, integrated with a heating element, to provide a unified environment for both incubation and visualization. This system enables MTB detection in a single step—requiring only sample loading—and produces robust, distinguishable fluorescence signals within 15 min (Figure 1). Collectively, this work provides a practical and low-cost pathway toward realized, fully integrated CRISPR-based POC diagnostics.

2. METHODS

2.1. Fabrication of Paper-Based Microfluidic Devices

Microfluidic patterns were designed using AutoCAD 2023 (Autodesk, USA) and fabricated on Whatman No. 1 filter paper (Whatman, USA). To evaluate the efficacy of different hydrophobic boundaries, two printing modalities were utilized: (i) a laser printer (HP Laser MFP 135a, HP, Thailand) utilizing thermoplastic toner, and (ii) a thermal transfer printer (MT800 2.0, HPRT, Germany) utilizing a carbon-wax ribbon.[15]

Postprinting, the devices underwent thermal incubation in a hot-air oven (Binder, Germany) to induce hydrophobic agent reflow and penetration into the cellulose matrix (Figure 2). For thermal transfer printing, temperatures of 90 °C, 120 °C, 150 °C, and 180 °C were evaluated. For laser printing, the ranges were optimized at 150 °C, 180 °C, 230 °C, and 260 °C. All samples were baked for 15 min and cooled to ambient temperature for at least 5 min prior to fluidic characterization.

2.2. Thermal and Fluidic Optimization

To maintain the stable 39 °C incubation required for CRISPR-Cas12a activity, three materials were evaluated as heat-conducting intermediates: an aluminum grate, aluminum foil, and poly(methyl methacrylate) (PMMA). Surface temperature profiles were recorded using an MLX90640 infrared thermal imaging camera (Waveshare, China) to assess heating uniformity and steady-state stability.

To characterize flow dynamics, 10 μL of aqueous red dye was applied to the inlet of μPADs placed on a heat block (Four E's, China) at 39 °C. The capillary front progression was recorded for 15 min via smartphone (iPhone 16 Pro Max, Apple Inc.), and wicking distances were quantified at 1 min intervals using ImageJ software (v1.53, NIH, USA). Experimental data ($n = 6$) were compared against four theoretical frameworks: (1) The classical Lucas-Washburn (LW) model,[16] (2) the LW model incorporating thermal evaporation,[17] (3) the Modified Lucas-Washburn (MLW) model accounting for boundary resistance,[18] and (4) a hybrid MLW model incorporating both boundary resistance and evaporation.[17,18] Model fitting and regression analysis were performed using MATLAB (R2024b, MathWorks, USA). Detailed equations and parameter constants are provided in the Supporting Information.

https://doi.org/10.1021/acsomega.6c00845
ACS Omega 2026, 11, 31169−31181

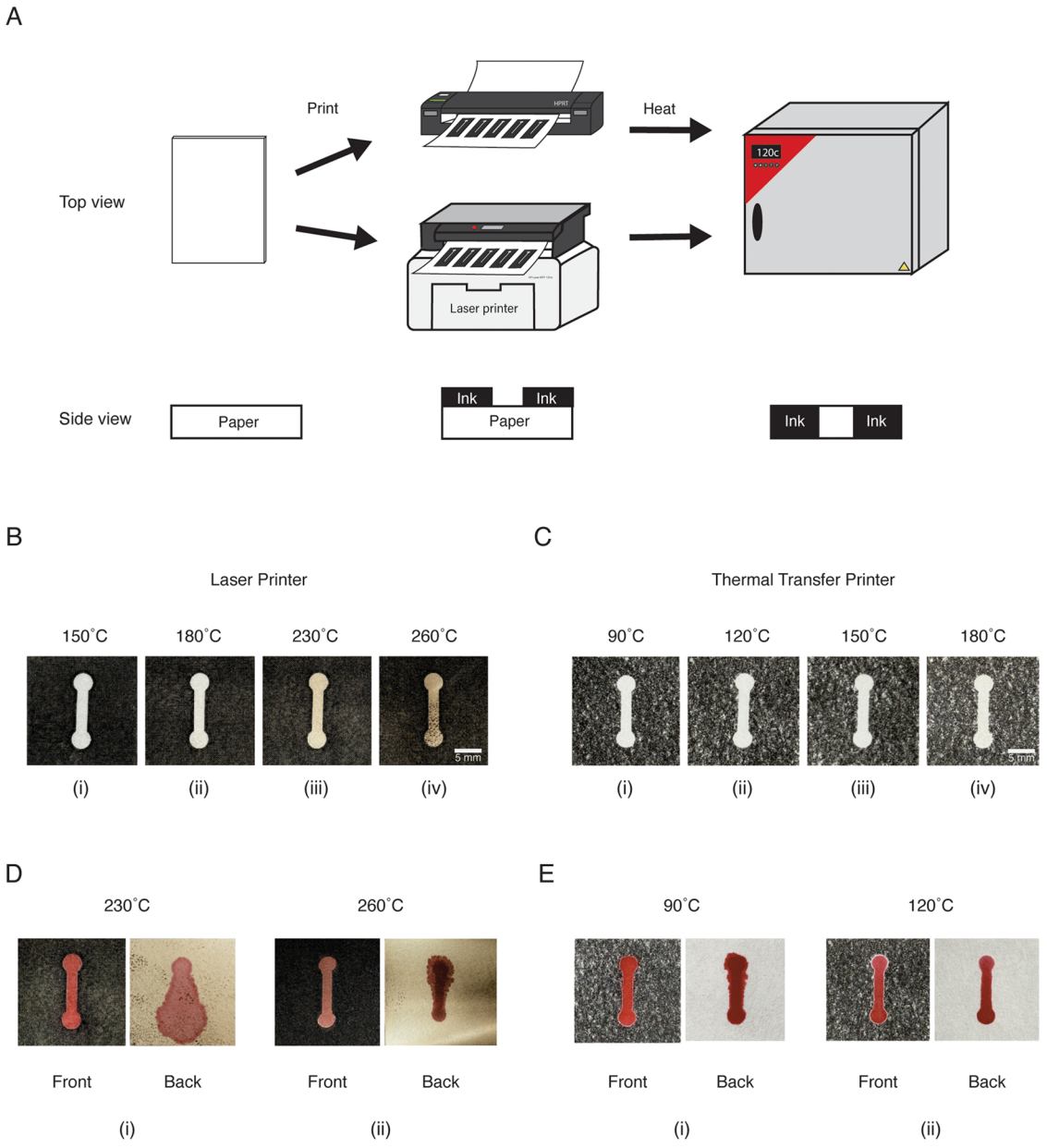


Figure 2. Fabrication and characterization of paper-based microfluidic barriers using laser and thermal transfer printing. (A) Schematic of the fabrication process. Hydrophobic ink was deposited onto cellulose paper via thermal transfer or laser printing, followed by thermal incubation to induce ink reflow and establish hydrophobic barriers. (B, D) Devices fabricated via laser printing at temperatures ranging from 150−260 °C. (D) Front and rear views of the devices showing significant liquid leakage through the paper substrate, even at high-temperature baking (230−260 °C). (C, E) Devices fabricated via thermal transfer printing at 90−180 °C. (E) Performance validation showing superior fluid containment with minimal leakage at 90 °C and complete barrier integrity at 120 °C across both front and back surfaces.

2.3. Fluorescence Reporter Optimization

Two fluorophore-quencher (FQ) probes, 6-FAM-BHQ1 and ROX-BHQ2, were compared to determine the optimal signal-to-background ratio on cellulose-based Whatman No.1 paper. Standard 10 μL CRISPR-Cas12a reactions consisted of: 50 nM EnGen Lba Cas12a (New England Biolabs, USA), 50 nM gRNA targeting *M. tuberculosis* (MTB) (Macrogen, South Korea), 1× NEBuffer r2.0 (New England Biolabs, USA), 400 nM FQ-probe (Macrogen, South Korea), and 3.35 ng/μL MTB DNA template. gRNA and template sequences were derived from previous study.[19]

Reactions were initially performed in 0.2 mL microtubes at 39 °C for 15 min. Subsequently, 10 μL aliquots were deposited onto paper microspots and visualized using a UV transilluminator (Major Science, USA). Images captured under identical exposure settings were processed in ImageJ. To correct for uneven excitation and substrate interference, RGB images were split into channels; the signal channel (Red for ROX; Green for FAM) was normalized against the Blue channel (the paper background/excitation reference).

2.4. Integrated On-Chip CRISPR-Cas12a Assay

To minimize nonspecific binding, μPAD inlets were blocked with 3.6 μL of 1% BSA and dried at 37 °C for 60 min. A CRISPR master mix—comprising 100 nM Cas12a, 100 nM gRNA, 800 nM ROX-BHQ2 probe, and 1% sucrose as a lyoprotectant in 1× NEBuffer r2.0—was preincubated at room temperature for 20 min to allow ribonucleoprotein (RNP) complex formation. A 4.67 μL aliquot of this mix was deposited into the inlet and air-dried for 60 min.

The diagnostic was initiated by adding 10 μL of MTB DNA (0.0335−3.35 ng/μL) to the inlet. Devices were mounted on a PMMA base and incubated at 39 °C. Fluorescence was monitored at

https://doi.org/10.1021/acsomega.6c00845
ACS Omega 2026, 11, 31169−31181

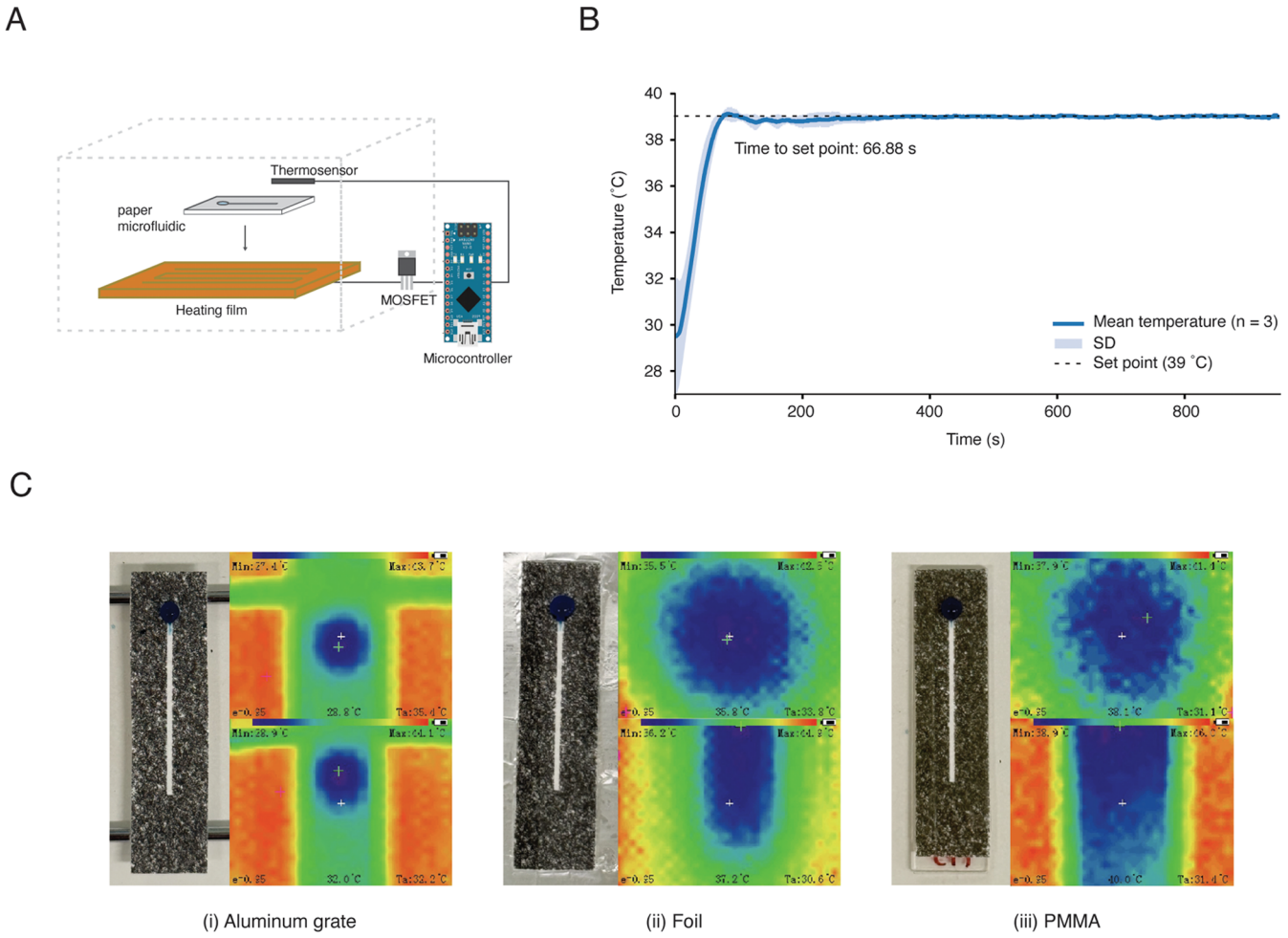


Figure 3. Design and characterization of the temperature control system for isothermal CRISPR incubation. (A) Schematic of the custom thermal control module. A polyimide heating element provides heat to the paperfluidic device, regulated by a closed-loop system. A microcontroller monitors real-time temperature via a sensor in contact with the paper and adjusts the heater output through a MOSFET. (B) Temporal temperature profile recorded by a thermocouple, demonstrating stable maintenance of the 39 °C set point over time. (C) Comparison of thermal gradients across paperfluidic channels when using (i) aluminum grate, (ii) aluminum foil, and (iii) PMMA as heat-conducting substrates at a 39 °C set point.

5 min intervals using the UV transilluminator and normalized via the ImageJ ratiometric method described above.

Final end point signals at 30 min were validated using a fluorescence microscope (Motic PX43 FS46) equipped with a TRITC filter set (Ex: 540/25 nm, 565 nm dichroic, Em: 605/55 nm). Signal distribution and intensity were analyzed to confirm the correlation between the portable readout and high-resolution microscopy.

2.5. Development of Integrated Opto-Thermal Hardware

2.5.1. Closed-Loop Thermal Control Module. To ensure a stable 39 °C environment for the CRISPR-Cas12a assay, a compact, custom heating module was developed. The thermal source consisted of a 12 V 49 mm × 19 mm polyimide flexible heater (Electric, China) was selected for its rapid thermal response and uniform heat distribution. The heater was bonded to a custom sample holder within a 3D-printed housing using GD9980 thermal conductive adhesive to minimize interfacial thermal resistance.

Temperature regulation was managed by an Arduino Uno R3 microcontroller (Arduino, Italy) utilizing a Proportional-Integral-Derivative (PID) control algorithm. Real-time thermal feedback was provided by a DS18B20 digital temperature sensor (±0.5 °C accuracy) positioned in direct contact with the sample plane. The Arduino modulated power delivery to the heater via an IRL2203N N-channel MOSFET driven by pulse-width modulation (PWM). Surface temperature uniformity was validated using a FLIR ONE Gen 3 infrared camera, confirming consistent heat distribution across the μPAD substrate throughout the 15 min incubation period.

2.5.2. Fluorescence Excitation and Imaging Module. A custom fluorescence module was engineered to provide uniform excitation for the ROX-based reporter probes. The excitation source comprised a high-power LED array (ILH-OP04-TRGR-SC221-WIR200, OSRAM, Germany) with a dominant emission peak at 525 nm. To ensure spatial uniformity of illumination, each of the four LEDs—positioned at the corners of the 3D-printed housing—was covered with an optical diffusing layer. In the detection path, a 650 nm long-pass emission filter (HB650, Tangsinuo, China) was integrated to suppress scattered excitation light and selectively transmit the fluorescence signal. The optical output was characterized using a calibrated power meter (PM100D2, Thorlabs, USA), yielding a stable power density of approximately 10 mW at the sample plane.

Electronic control was facilitated by an ESP32 microcontroller (Espressif Systems, China) coupled with a constant-current LED driver (LDB-350L, Mean Well, Taiwan) to ensure stable optical output independent of voltage fluctuations. User interaction, including real-time adjustment of excitation intensity, was implemented via an incremental rotary encoder (EC12D1564404, Alps Alpine, Japan). To manage the thermal load generated by the high-power LEDs during prolonged operation, an active cooling system—comprising an aluminum heat sink (TO220, 20 mm × 15 mm × 10

https://doi.org/10.1021/acsomega.6c00845
ACS Omega 2026, 11, 31169−31181

mm) and a DC axial fan (12 V DC, 30 mm × 30 mm × 10 mm)—was integrated. This cooling system was regulated by a logic-level N-channel MOSFET (IRLZ44NPBF, Infineon, Germany) to maintain hardware stability without interfering with the optical excitation circuitry.

3. RESULTS AND DISCUSSION

3.1. Optimization of Hydrophobic Barrier Fabrication via Laser and Thermal Transfer Printing

μPADs are frequently fabricated using hydrophobic patterning due to its simplicity and compatibility with cellulose substrates.[20,21] Following the discontinuation of commercial wax printers,[22,23] laser and thermal transfer printing have emerged as cost-effective, accessible alternatives.[15,24] In this study, we evaluated the barrier quality and thermal requirements of a laser printer (HP Laser MFP 135a) using styrene-acrylate toner and a thermal transfer printer (HPRT MT800 2.0) using carbon ribbon. To assess the performance, a microfluidic channel was printed onto Whatman No. 1 filter paper and baked at temperatures ranging from 150−260 °C for laser-printed devices and 90−180 °C for thermal transfer-printed devices to induce ink penetration (Figure 2A).

Laser printing initially produced high-resolution, sharp hydrophobic patterns (Figure 2B). However, establishing a complete vertical barrier required melting the toner to penetrate the cellulose matrix. Most commercial black toners are composed of styrene−acrylate copolymers or polyester resins (85−90%) which typically soften only between 150−200 °C.[24,25] Consequently, extreme baking temperatures were necessary to facilitate resin flow into the paper fibers.

We observed that temperatures below 230 °C were insufficient to achieve full penetration. Even at 260 °C for 15 min, the hydrophobic barriers remained permeable, resulting in significant dye leakage (Figure 2D). Furthermore, the high thermal energy required for toner reflow induced pyrolysis of the cellulose, causing visible browning and structural degradation of the paper. This thermal damage compromised the fiber network, creating pathways for liquid to bypass the intended channels.[26] Further optimization suggested that double printing and lengthening of baking time to 60 min can prevent leakage, but paper browning remained (Supporting Figures S1−S3). Thus, while laser printing offers high spatial resolution, the high melting point of its thermoplastic components poses a significant risk of substrate damage and barrier failure.

In contrast, thermal transfer printing yielded lower-resolution patterns but superior functional performance (Figure 2C). This success is attributed to the composition of the carbon ribbons, which utilize wax or wax−resin blends that melt at significantly lower temperatures (70−110 °C and 120−160 °C, respectively) than laser toner.[27]

Experimental results indicated that while a 90 °C bake initiated barrier formation, it resulted in minor leakage (Figure 2E.i). Increasing the temperature to 120 °C allowed the molten wax to fully saturate the cellulose fibers, creating a robust, leak-proof hydrophobic boundary (Figure 2E.ii). Because these temperatures are well below the threshold for paper degradation, the structural and chemical integrity of the μPAD was preserved without discoloration or brittleness.

While laser printing provides higher initial resolution, its high-temperature requirements lead to incomplete barriers and substrate damage. Thermal transfer printing, despite lower pattern fidelity, ensures superior fluid containment and preserves paper integrity due to the favorable reflow properties of wax-based inks. Based on these findings, we selected thermal transfer printing followed by baking at 120 °C for 15 min as the optimized fabrication protocol.

3.2. Development and Optimization of the Thermal Control Module for Isothermal Incubation

Precise temperature regulation is critical for CRISPR-Cas12a diagnostics, as the enzyme's trans-cleavage activity requires stable incubation at 39 °C.[28] To facilitate portable, point-of-care testing, we developed a compact, closed-loop thermal control module. This system integrates a polyimide heating film, a MOSFET-driven power stage, and a microcontroller that monitors real-time temperature via a thermal sensor in contact with the paperfluidic device (Figure 3A). We confirmed that this custom heater maintains a stable 39 °C set point with minimal fluctuation over extended durations (Figure 3B).

A significant challenge in paper-based reactions is the direct interaction between the heat source and the porous substrate. Increasing the temperature typically reduces the interfacial tension of the liquid, which weakens capillary forces and can lead to uncontrolled wicking or leakage.[29] To mitigate these thermal−capillary effects and ensure uniform heat distribution without compromising fluidic confinement, we evaluated three materials as thermal intermediates: (i) an aluminum grate, (ii) aluminum foil, and (iii) poly(methyl methacrylate) (PMMA).

The aluminum grate was initially tested for its high thermal conductivity. However, it demonstrated the poorest thermal performance. Infrared thermography revealed that the reservoir and flow channels reached only 27.4 and 28.9 °C, respectively—well below the 39 °C target (Figure 3C.i). This discrepancy is attributed to the grate's discontinuous geometry, which minimized direct conductive contact. Consequently, heat transfer was dominated by air-gap convection rather than solid-state conduction, leading to inefficient heating and significant thermal gradients.[30]

Next, we evaluated aluminum foil to maximize the contact surface area. The paper device was rolled tightly onto a sheet of aluminum foil to promote conformal contact and conductive transfer. While this improved temperatures in the reservoir (35.5 °C) and flow channel (36.2 °C), the distribution remained nonuniform (Figure 3C.ii). The foil achieved the target temperature only at the edges where it was mechanically secured with adhesive tape. In the central regions, microscopic gaps and surface roughness between the foil and the paper increased thermal contact resistance, obstructing uniform equilibration.[31,32]

Finally, PMMA was evaluated as a rigid intermediate. Despite having lower thermal conductivity than aluminum, PMMA provided a stable, planar interface that ensured consistent mechanical coupling across the entire device. Under these conditions, the reservoir and flow channel reached 37.9 and 38.9 °C, respectively, successfully approaching the required 39 °C set point (Figure 3C.iii).

Unlike the aluminum foil, the dimensional stability of PMMA prevented deformation or wrinkling during heating. This rigidity eliminated irregular contact interfaces, ensuring continuous conductive heat transfer across the paper porous membrane.[33] Based on these results, PMMA was selected as the optimal thermal intermediate for the integrated CRISPR-Cas12a platform.

https://doi.org/10.1021/acsomega.6c00845
ACS Omega 2026, 11, 31169−31181

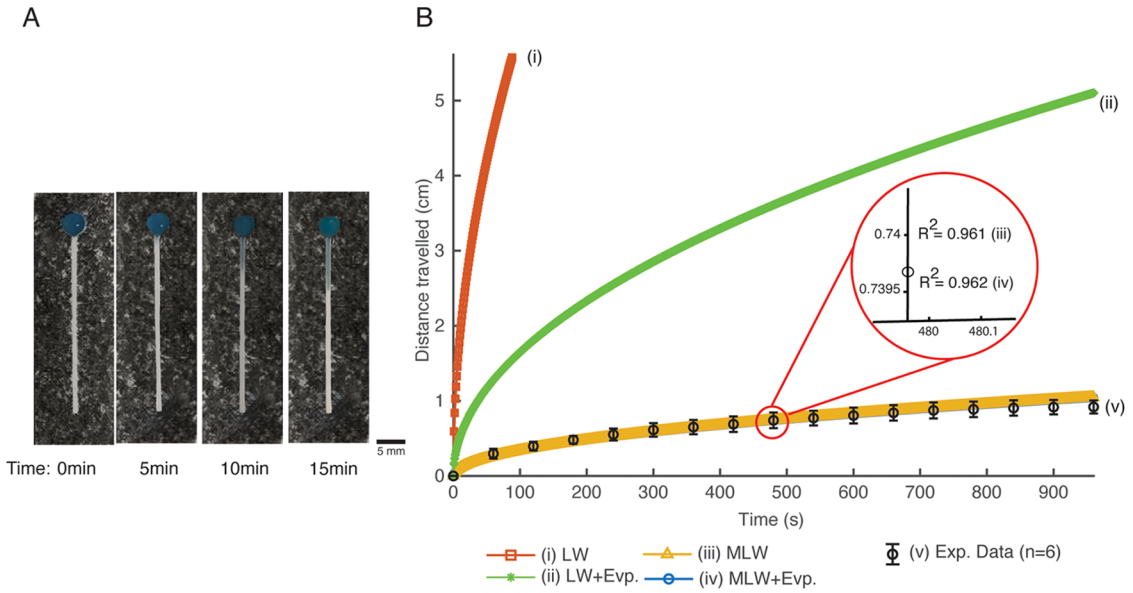


Figure 4. Mathematical modeling and experimental characterization of liquid wicking in paper-based channels. (A) Time-lapse images documenting the capillary flow of colored water through the paperfluidic device over a 15 min period. (B) Capillary wicking kinetics showing (v) experimental flow distance (mean ± SD, $n = 6$) compared against four predictive mathematical models: (i) the Lucas-Washburn (LW) model, (ii) LW with evaporation (LW + Evp.), (iii) the Modified Lucas-Washburn (MLW) model, and (iv) MLW with evaporation (MLW+Evp.). Due to their high degree of convergence, the MLW and MLW + Evp profiles are virtually indistinguishable at the primary scale, with the MLW + Evp curve obscured by the MLW line. The inset (magnified in the red circle) reveals the MLW + Evp model is situated marginally below the MLW line, reflecting the accounted evaporative loss.

3.3. Mathematical Modeling and Fluidic Design for Autonomous Assay Timing

A complete CRISPR−Cas12a assay requires a 15 min isothermal incubation to achieve optimal target recognition and trans-cleavage activity. To develop a self-contained point-of-care platform, we designed the channel geometry such that the reaction mixture wicks through the device over this 15 min interval. This allows the paperfluidic architecture to function as an integrated timing mechanism, eliminating the need for external timekeeping. To achieve this, we characterized the liquid wicking kinetics within the hydrophobic-patterned cellulose and evaluated several mathematical models to predict flow dynamics and determine the appropriate channel length.

Experimental wicking distances in Whatman-based paperfluidics were measured over 15 min ($n = 6$, Figure 4A), exhibiting the characteristic deceleration typical of capillary-driven flow in porous media. We first applied the classical Lucas−Washburn (LW) equation, which relates imbibition distance to time in a simplified capillary network. However, the LW model significantly overestimated the experimental flow distances Figure 4B, curve (i). This discrepancy occurs because the LW formulation assumes an unconfined, homogeneous pore network with uniform radii and disregard potential effects of evaporation.[16] In reality, evaporation can affect capillary flow especially with small liquid volumes at elevated temperatures, and the printed hydrophobic boundaries in μPADs restrict lateral expansion and introduce significant hydrodynamic resistance, which reduces the effective capillary driving pressure and slows the flow front.

Given that the CRISPR−Cas12a assay is conducted at 39 °C, we evaluated the role of evaporation as a potential modifier of wicking velocity. Using a model that incorporates evaporative mass loss and environmental conditions,[17] we found that the evaporation-dependent term (Evp) predicted lower imbibition distances than the standard LW model Figure 4B, curve (ii). However, these predictions remained considerably higher than the experimental data. This suggests that while evaporation is measurable at 39 °C, it is a secondary factor compared to the dominant resistance imposed by the physical channel boundaries.

To account for the hydrodynamic constraints of channel confinement, we applied the Modified Lucas−Washburn (MLW) model. This model accounts for the counteracting interfacial forces produced by the surface tension along the hydrophobic boundaries, which oppose the forward movement of the meniscus.[18] In the 1 mm channel width utilized here—a common dimension in μPAD design[34−36] these boundary effects are particularly pronounced. The MLW model closely reproduced the experimental wicking behavior across all time points (Figure 4B, curve iii, $R^2 = 0.961$). This confirms that boundary-induced resistance, rather than evaporation or intrinsic pore heterogeneity alone, is the primary determinant of flow dynamics in patterned paper channels.

Finally, we constructed a hybrid model combining the MLW boundary term with the evaporation term to ensure broad applicability. The resulting curve Figure 4B, curve (iv) was nearly indistinguishable from the MLW prediction, as shown by the high degree of overlap in the primary plot. A slight reduction in flow distance is only observable in the magnified inset (Figure 4B, inset), and the model fit improved only marginally ($R^2 = 0.962$). At 15 min, the model predicts the final imbibition distance to be 10.452 mm.

The results demonstrate that hydrophobic boundary resistance is a dominant physical factor controlling capillary transport within the wax-patterned paper channels, with evaporation playing a comparatively minor role under the present conditions. Despite a minor role played by evaporation, the hybrid model (MLW + evaporation) remains applicable should future device versions operate at higher

https://doi.org/10.1021/acsomega.6c00845
ACS Omega 2026, 11, 31169−31181

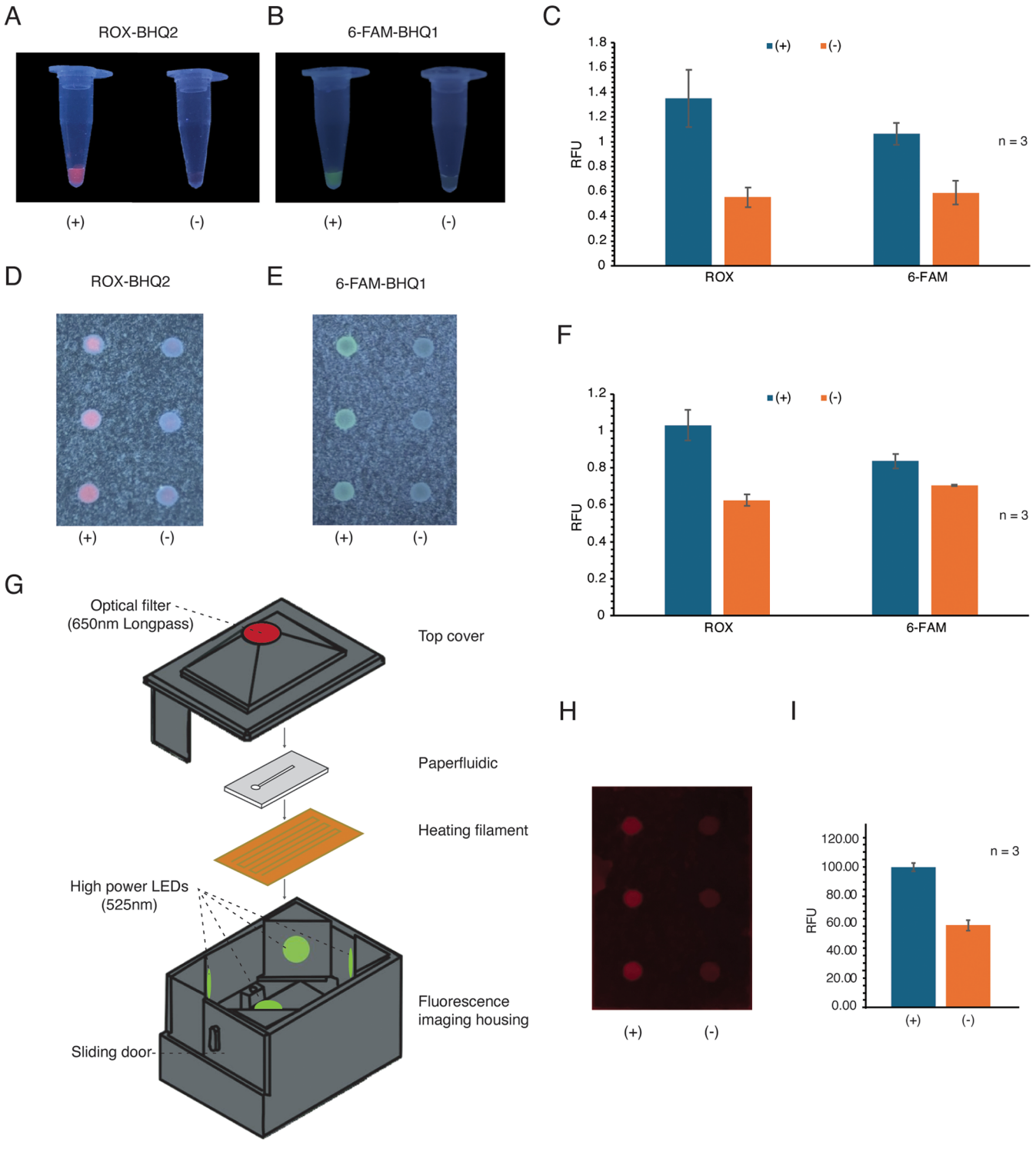


Figure 5. Optimization and hardware integration of the CRISPR fluorescence readout on paperfluidics. (A−B) Representative fluorescence images of MTB CRISPR assays performed in microtubes using (A) ROX-BHQ2 and (B) 6-FAM-BHQ1 fluorophore-quencher reporter probes. (C) Quantitative comparison of fluorescence intensities in microtubes. (+) and (−) denote the positive control (with MTB template) and negative control (no-template control), respectively. (D−E) Fluorescence visualization of the CRISPR assay when deposited on cellulose-based paper using (D) ROX-BHQ2 and (E) 6-FAM-BHQ1. (F) Comparative analysis of signal performance on paper, highlighting the superior signal-to-background ratio of the ROX-BHQ2 probe. (G) Schematic of the integrated 3D-printed opto-thermal module. The system features a light-tight enclosure, four high-power green LEDs (λ = 525 nm) for excitation, and a 650 nm long-pass emission filter. The polyimide heating element (from Figure 2) is integrated into the base for simultaneous incubation and real-time visualization. (H) Fluorescence images of MTB CRISPR assays captured within the custom module using the optimized ROX-BHQ2 probe. (I) Fluorescence intensity quantification of the diagnostic results obtained using the integrated imaging system.

https://doi.org/10.1021/acsomega.6c00845
ACS Omega 2026, 11, 31169−31181

temperatures, longer durations, or under lower humidity, where evaporation becomes non-negligible. This model-driven approach ensures that our μPAD provides a deterministic 15 min reaction window, enhancing the reliability and autonomy of the diagnostic platform.

Beyond its role as an intrinsic timer, this modeled capillary channel synchronizes three essential phases of the diagnostic workflow: (1) The controlled rehydration and initiation kinetics of the prestored reagents at the inlet, (2) the maintenance of convective mixing as the sample front traverses the reservoir, and (3) the regulation of the effective incubation period, ensuring the Cas12a-gRNA complex has sufficient contact time with the target DNA sample.

To ensure the reliability of this timing mechanism, we utilized Whatman No. 1 paper as the substrate due to its highly uniform porosity and pore size distribution. Our experimental validation demonstrated that the wicking velocity and resultant arrival times at the terminus vary by less than 10% across independent trials (Supporting Figure S4). This degree of fluctuation ensures that mixing efficiency and reagent contact time remain within an acceptable functional window. Consequently, the hybrid model-driven design (MLW + evaporation model) on a standardized Whatman No. 1 substrate provides a robust and reliable architecture for our subsequent autonomous CRISPR-based detections.

3.4. Optimization of CRISPR-Cas12 Reaction and Opto-Thermal Module Integration

To ensure robust performance upon integration into the paper-based microfluidic device, the CRISPR−Cas12a reaction was optimized to maximize fluorescence discrimination under both tube-based and paper-based conditions.

3.4.1. Fluorescence Signal Optimization. While CRISPR−Cas12a biochemistry is relatively standardized, the choice of the single-stranded DNA fluorescence−quencher (ssDNA-FQ) reporter can significantly impact sensitivity. Most conventional assays utilize 6-FAM−BHQ1 due to its high quantum yield and compatibility with standard laboratory equipment.[37,38] However, cellulose-based substrates present unique optical challenges. In initial tube-based assays, the 6-FAM reporter provided a clear distinction between positive (MTB DNA) and negative controls, yielding a 1.80-fold signal ratio (Figure 5B,C). However, when the reaction was transferred to cellulose paper, this contrast was severely attenuated to ∼1.18-fold (Figure 5E,5F). This impaired performance is attributed to the strong autofluorescence of cellulose in the blue−green spectral region (λ < 550 nm), which overlaps with the 520 nm emission peak of 6-FAM.[39] This spectral overlap increases background noise and masks the Cas12a-generated signal, significantly reducing the signal-to-noise ratio (SNR).

To mitigate this, we evaluated a red-shifted reporter, ROX−BHQ2. ROX emits in the 580−750 nm range, a spectral window where cellulose autofluorescence is minimal. In tube-based assays, the ROX reporter outperformed 6-FAM with a 2.45-fold signal contrast (Figure 5A,C). On paper, the ROX signal maintained a substantial contrast of ∼1.65-fold (Figure 5D,5F). Beyond spectral selection, we optimized the architecture of the ssDNA-FQ probe by evaluating the influence of linker length (6-mer vs 10-mer) and base sequence on signal output.[40] Our results demonstrated that a 10-mer linker with an optimized sequence yielded a 2.5-fold improvement in the signal-to-noise (S/N) ratio compared to shorter variants (Supporting Figure S5). This enhancement likely stems from a superior balance between quenching efficiency in the intact state and increased steric accessibility for Cas12a-mediated cleavage upon target recognition. This improvement confirms that red-shifting the reporter fluorophore and additional optimization of the probe sequence are essential for reliable diagnostic readout on paper, as it minimizes background interference and enhances Cas12a cleavage activity.

To further facilitate point-of-care diagnostics, we developed a compact, 3D-printed fluorescence imaging module (Figure 5G). The system features a light-tight housing equipped with four high-power green LEDs (λ = 525 nm) positioned at the corners to provide uniform excitation. A 650 nm long-pass emission filter is integrated into the top cover to attenuate excitation light and selectively transmit the ROX fluorescence signal. Furthermore, the polyimide heating element (detailed in Results Section 2) was incorporated into the base of the module. This integration allows the device to function as a unified platform for both the 39 °C isothermal incubation and the real-time visualization of the CRISPR assay. Validation experiments showed that this custom module provides a signal contrast between positive and negative controls comparable to that of a commercial transilluminator (Figure 5H−I), confirming its utility as a low-cost, portable diagnostic reader.

While the integration of electronic components increases the internal complexity of the device, it significantly reduces the workflow burden on the end-user compared to conventional tube-based CRISPR assays. Traditional tube-based methods are labor-intensive, requiring separate heating blocks, manual timing, and physical transfer to a UV/blue light imaging station—steps that introduce thermal fluctuations and potential for operation error. Our platform consolidates these disparate steps into a single, closed-loop environment. By internalizing the thermal and optical controls, the user interface is simplified to two discrete toggle actions: initiating the heater and activating the LED for readout. This approach replaces multiple manual interventions with two automated steps, significantly simplifying the diagnostic workflow.

3.4.2. Optimization of CRISPR-Cas12a System. Prior studies suggest that target sequence and gRNA characteristics, including amplicon length, GC content and secondary structure, may affect the sensitivity of the assay performance. Our findings indicate that the physical length of the DNA template has a negligible effect on trans-cleavage kinetics. Specifically, we observed comparable fluorescence signals when using a 330 bp PCR product versus a 3000 bp plasmid template (data not shown). This suggests that once the Cas12a-gRNA complex identifies the Protospacer Adjacent Motif (PAM) and initiates strand displacement, the distal length of the DNA does not interfere with enzymatic activation.

In contrast, GC content of the target sequence significantly influences Cas trans-cleavage activity. High GC content (>60%) can hinder the "unzipping" of dsDNA, while low GC content (<20%) can destabilize the crRNA−target hybrid.[41] The GC content of the MTB target used in this study is approximately 60%, the upper bound of this preidentified functional range. By demonstrating robust Cas12a activity at this high-GC threshold, we establish that our platform is thermodynamically versatile enough to handle the vast majority of human pathogens and model organisms,

https://doi.org/10.1021/acsomega.6c00845
ACS Omega 2026, 11, 31169−31181

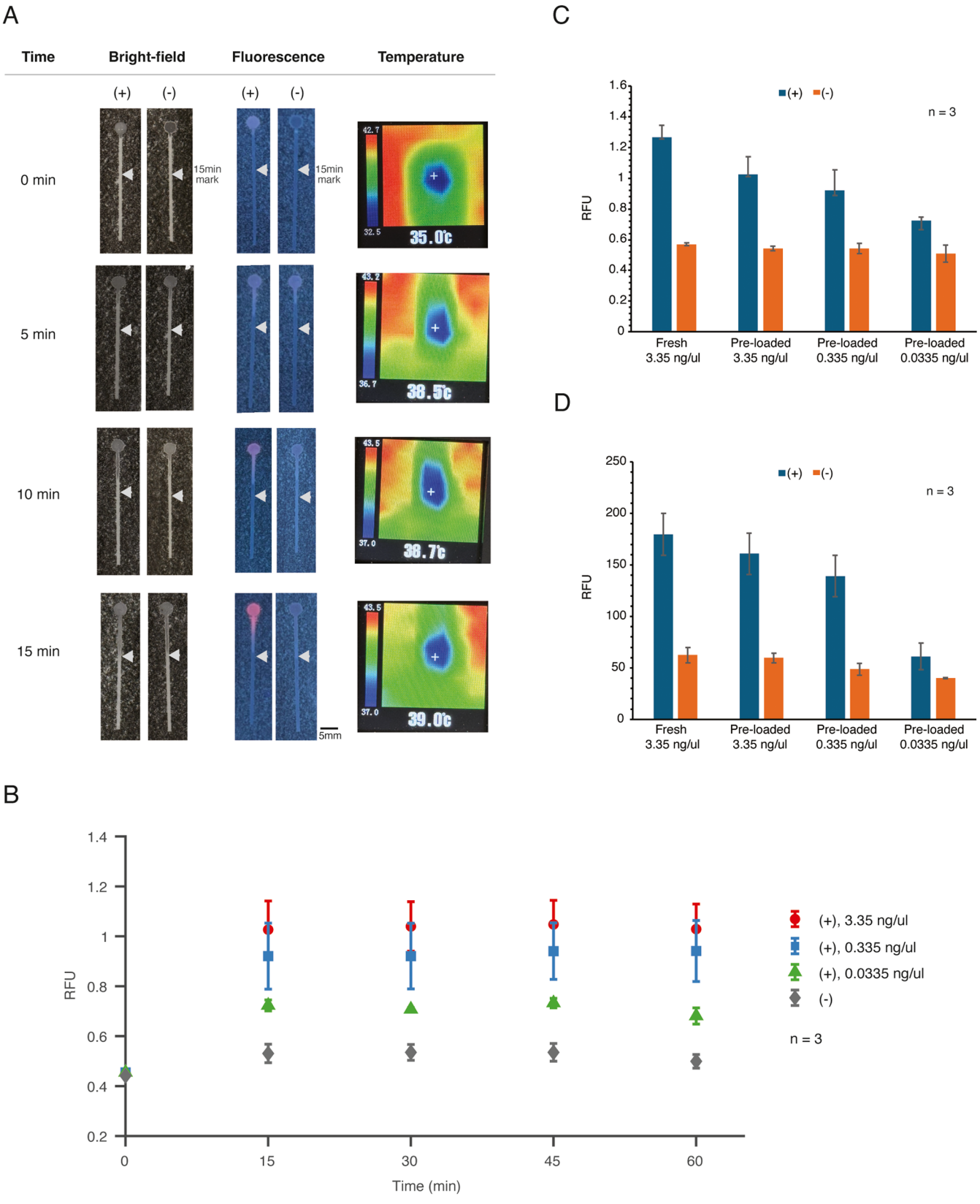


Figure 6. Integrated on-chip CRISPR-based detection of *Mycobacterium tuberculosis* (MTB). (A) Representative bright-field, fluorescence, and thermal distribution profiles of the diagnostic assay performed entirely on the paperfluidic platform at 0, 5, 10, and 15 min. (B) Temporal fluorescence kinetics for varying MTB template concentrations (0, 0.0335, 0.335, and 3.35 ng/μL), demonstrating concentration-dependent signal amplification. (C−D) End point quantitative fluorescence analysis at 30 min, comparing the performance of freshly prepared master mix versus prestored (dried) reagents at three template concentrations. Results were validated using (C) a commercial transilluminator and (D) a fluorescence microscope to confirm the reliability of the paper-stored chemistry.

https://doi.org/10.1021/acsomega.6c00845
ACS Omega 2026, 11, 31169−31181

Table 1. Comparative Cost and Infrastructure Analysis of the Proposed Platform, Tube-Based CRISPR, and Conventional qPCR.[44−48]

feature	conventional qPCR	tube-based CRISPR	this Platform
Consumable Cost (per test)	$12−30	$1−10	$0.5−5
Reaction Volume (per reaction)	20−50 uL	20 uL	10 uL
Required Equipment	Real-time PCR System	Heat block + Imager	Integrated Device
Equipment Cost	$15,000−$25,000	$500−$1,000	$100

which typically reside in the more accessible 30−60% GC range.[42]

Complementary to target accessibility, the secondary structure of the gRNA was also optimized. Given that internal hairpins with more than three complementary base pairs can significantly impair hybridization kinetics,[41] our gRNA design was restricted to a minimal 3 bp hairpin. This balance of parameters ensures that the assay remains robust against the typical genomic variations found in M. tuberculosis isolates.

Beyond thermodynamic and structural considerations, the diagnostic specificity of the gRNA was a primary design criterion. The spacer sequence targeting the rpoB gene was selected based on its proven high-fidelity performance in discriminating MTB from closely related species. Previous validation of this specific gRNA architecture against a panel of seven nontuberculous mycobacteria (NTM) strains demonstrated 100% specificity, with no observed cross-reactivity.[19] By utilizing this validated biological foundation within our integrated platform, we ensure that the paper-based reaction environment maintains the molecular precision required for differentiation among the closely related tuberculosis species.

3.5. Validation of On-Chip CRISPR−Cas12a for MTB Diagnostics

We validated the integrated platform by performing a complete CRISPR−Cas12a assay for *M. tuberculosis* (MTB) detection directly on the developed μPAD.

3.5.1. Reagent Stabilization and On-Device Performance. To facilitate a "ready-to-use" diagnostic format, the CRISPR master mix—including a 1% sucrose lyoprotectant—was prestored and dried within the μPAD inlet reservoir. Sucrose preserves the structural and catalytic integrity of the Cas12a enzyme during dehydration, allowing for ambient storage and simplified operation in the field.[43]

Upon the addition of MTB DNA and incubation at 39 °C, the prestored reagents were successfully reconstituted, initiating target-activated collateral cleavage. Fluorescence intensified progressively over the 15 min wicking period (Figure 6A,B). Quantitative analysis showed that prestored reagents retained over 85% of the activity seen in freshly prepared reactions, with a signal-to-background ratio of 1.90-fold compared to 2.22-fold for fresh mix (Figure 6C). This confirms that our platform supports the effective activation of dried CRISPR components, significantly enhancing its practicality for decentralized applications.

3.5.2. Analytical Sensitivity and Kinetic Profile. The analytical performance of the integrated system was evaluated across a range of MTB DNA concentrations (0.0335 to 3.35 ng/μL). Fluorescence for the two higher concentrations reached saturation within 15 min, indicating rapid reporter turnover (Figure 6B). While the lowest concentration (0.0335 ng/μL) exhibited a slower signal progression, it remained clearly distinguishable from the no-template control at the 15 min end point, establishing it as the limit of detection (LOD) for the integrated μPAD.

Interestingly, incubation beyond 30 min led to a minor decrease in fluorescence intensity. This is likely due to photobleaching of the ROX fluorophore from repeated excitation during measurement and thermal degradation over time. These results validate the 15 min "intrinsic timer" design, which provides the optimal balance between maximum signal intensity and rapid diagnostic turnaround.

In addition, while minor timing fluctuations can influence the absolute fluorescence intensity, our results indicate that the platform remains robust; a 10% variance in timing, the maximum variance observed in the fluidic flow on our platform (discussed in Section 3), does not compromise the ability to distinguish between positive and negative controls, maintaining a statistically significant signal-to-noise ratio (SNR).

3.5.3. Comparison of Fluorescence Readout Modalities. Finally, we compared the performance of our μPAD across different imaging systems to assess its adaptability to various settings. While a fluorescence microscope provided the highest signal-to-background ratios (1.5- to 2.90-fold) (Figure 6D) due to its precise narrow-band filters, its cost and complexity are prohibitive for point-of-care use.

In contrast, more accessible methods like a commercial UV transilluminator or our custom imaging module (detailed in Results Section 4) yielded lower but sufficient contrast ratios (1.42- to 1.90-fold) for clear positive/negative discrimination. The ability to achieve reliable results across different optical setups—from high-end microscopy to simple portable transilluminators—demonstrates the robustness of the ROX-based μPAD platform for both clinical and field-based MTB diagnostics.

3.5.4. Optimization of μPAD and Detection Mechanism. The spatial configuration of the μPAD was engineered to synchronize fluidic transport with the CRISPR-Cas12a enzymatic kinetics. While fluorescence signal is detectable across the device, the circular inlet reservoir was designated as the primary readout zone for three critical reasons.

First, the downstream wicking into the capillary timing channel—governed by the Modified Lucas−Washburn parameters optimized in Section 3—induces a continuous convective flux. This wicking action facilitates the rapid and uniform rehydration of the predried CRISPR-Cas12a reagents (Cas12a-gRNA complex and reporters) within the reservoir. Unlike stationary droplet assays that rely on passive diffusion, this flow-driven mixing ensures intimate contact between the target DNA and the enzymatic machinery, effectively initiating the reaction.

Second, the porous matrix of the Whatman No. 1 paper exerts a molecular sieving effect. Given the high molecular weight and large hydrodynamic radius of the Cas12a-gRNA ribonucleoprotein (RNP) complex (160 kDa), its mobility through the cellulose fiber network is significantly lower than that of smaller nucleic acid fragments or reporter molecules. Consequently, at the 15 min diagnostic mark, the RNP complexes remain more concentrated within the reservoir.

https://doi.org/10.1021/acsomega.6c00845
ACS Omega 2026, 11, 31169−31181

This localized enrichment results in a superior signal-to-noise ratio (SNR) compared to the downstream channel.

Finally, the enlarged geometry of the reservoir (diameter = 3 mm) provides a stable optical window, which is more conducive to visual inspection and robust digital image capture than the narrow 1 mm wicking channel.

3.5.5. Economic Feasibility and Suitability for Resource-Limited Settings. A critical barrier to the decentralization of MTB diagnostics is the prohibitive cost of both capital equipment and specialized reagents. To evaluate the economic competitiveness of our platform, we conducted a comparative cost analysis against current diagnostic standards (Table 1)

The economic advantage of the proposed platform is 2-fold. First, the transition to a μPAD format enables a 2-fold reduction in reaction volume (20 to 10 μL) compared to standard tube-based CRISPR assays. This directly translates to lower expenditure on high-cost biochemical components. Second, our platform addresses the infrastructure gap by consolidating heating and imaging functions into a single, low-cost housing ($100). This represents a significant reduction in equipment costs compared to tube-based CRISPR and conventional qPCR systems. By eliminating the need for expensive, stationary laboratory hardware, this integrated opto-thermal system provides a scalable solution for MTB screening in decentralized healthcare centers where capital-intensive infrastructure is unavailable.

4. CONCLUSION

In this study, we have developed a fully integrated paper-based microfluidic platform (μPAD) for the rapid and autonomous detection of *Mycobacterium tuberculosis* using the CRISPR-Cas12a system. By systematically optimizing the fabrication process, we identified thermal transfer printing as the superior method for creating robust hydrophobic barriers that preserve the structural and chemical integrity of the cellulose substrate. Our integration of a closed-loop thermal control module with a PMMA intermediate ensured stable and uniform 39 °C incubation, effectively overcoming the thermal−capillary challenges inherent in heated paperfluidics.

The platform's functionality is further enhanced by a hybrid mathematical model of capillary wicking, which allowed for the design of an "intrinsic timer" that aligns the fluidic transport with the 15 min CRISPR reaction kinetics. To bridge the gap between laboratory results and field-deployable diagnostics, we designed and built a custom, compact fluorescence imaging module. This hardware—integrated with our specialized opto-thermal heating base—provides a unified environment for simultaneous incubation and high-contrast visualization of the ROX−BHQ2 reporter signal. By utilizing this red-shifted probe alongside our optimized gRNA and sucrose-based lyoprotection, we successfully mitigated paper autofluorescence and reagent instability and maintained high specificity, achieving a limit of detection of 0.0335 ng/μL with prestored reagents.

The integration between our custom-engineered opto-thermal hardware and the optimized paperfluidic architecture demonstrates that high-sensitivity molecular diagnostics can be transitioned from the laboratory to the point-of-care. This low-cost, user-friendly platform requires only a single sample-loading step and provides a visual readout within 15 min, making it highly suitable for decentralized testing in resource-limited settings.

While the current study validated the system using preamplified DNA, this platform possesses potentials for clinical sample testing. CRISPR-Cas systems have been validated on common clinical samples such as saliva, sputum, and plasma and proven to be resilient to common diagnostic inhibitors.[49,50] Only a brief preprocessing step involving chemical activation (e.g., RNase/DNase inhibitors) and a short heat-inactivation period is required prior to the CRISPR-Cas reaction to ensure sample compatibility. Given the inherent robustness of the CRISPR-Cas12a chemistry, this optimized platform possesses strong potential for direct application to clinical samples.

In addition, our paperfluidic design provides a foundational architecture for several future diagnostic advancements including one-pot diagnostics and alternative CRISPR/Cas systems. The opto-thermal module was specifically optimized to operate at 39 °C, a temperature compatible with both the CRISPR-Cas12a reaction and isothermal amplification techniques like RPA. This thermal alignment facilitates the future transition to a single-step, "one-pot" assay, where lysis, amplification, and detection occur within a single device.[51,52]

Beyond MTB detection, this system is intended as a universal diagnostic housing for diverse CRISPR-based technologies. Because the fluidic transport and mathematical modeling are based on the physicochemical properties of conserved components (e.g., gRNA, reporter probes, and Cas enzymes), these parameters are theoretically transferable to other systems, such as Cas13 for RNA detection, or amplification-free CRISPR-Cas systems.

Future work will explore the integration of high-sensitivity CRISPR cascades[53] or Cas12a2[54] variants capable of reaching attomolar detection limits without the need for upstream PCR or RPA and evaluate the platform's performance with clinical samples, moving one step closer to a truly field-deployable solution for global tuberculosis surveillance.

■ ASSOCIATED CONTENT

Supporting Information

The Supporting Information is available free of charge at https://pubs.acs.org/doi/10.1021/acsomega.6c00845.

> Comprehensive derivations of the mathematical models for capillary-driven flow in porous substrates, including the associated physical constants and parameter values used for MATLAB simulations (1), Figures S1−S3: extended optimization data for hydrophobic barrier fabrication using laser printing (2), Figure S4: comparative analysis of wicking consistency and flow dynamics between Whatman No. 1 and Double Ring 102 filter papers across multiple replicates (3), and Figure S5: sequence optimization of the ROX-functionalized fluorophore-quencher (FQ) ssDNA reporter probe (4) (PDF)

■ AUTHOR INFORMATION

Corresponding Author

Pimkhuan Hannanta-anan − *Department of Biomedical Engineering, School of Engineering, King Mongkut's Institute of Technology Ladkrabang, Bangkok 10520, Thailand;* orcid.org/0000-0002-9450-0799; Email: pimkhuan.ha@kmitl.ac.th

https://doi.org/10.1021/acsomega.6c00845
ACS Omega 2026, 11, 31169−31181

Authors

Aujchara Thepbut − *Department of Biomedical Engineering, School of Engineering, King Mongkut's Institute of Technology Ladkrabang, Bangkok 10520, Thailand*

Thitipa Rupprom − *Department of Biomedical Engineering, School of Engineering, King Mongkut's Institute of Technology Ladkrabang, Bangkok 10520, Thailand*

Lin T. Thant − *Department of Biomedical Engineering, School of Engineering, King Mongkut's Institute of Technology Ladkrabang, Bangkok 10520, Thailand*

Hein K. Nyein − *Department of Biomedical Engineering, School of Engineering, King Mongkut's Institute of Technology Ladkrabang, Bangkok 10520, Thailand*

Peeraphan Compiro − *Center of Excellence in Systems Microbiology (CESM), Department of Biochemistry, Faculty of Medicine, Chulalongkorn University, Bangkok 10330, Thailand*

Pornchai Kaewsapsak − *Center of Excellence in Systems Microbiology (CESM), Department of Biochemistry, Faculty of Medicine, Chulalongkorn University, Bangkok 10330, Thailand*

Complete contact information is available at: https://pubs.acs.org/10.1021/acsomega.6c00845

Notes

The authors declare no competing financial interest.

■ ACKNOWLEDGMENTS

The authors thank Dr. Sunchai Payungporn for access to biochemical reagents. This work is supported by King Mongkut's Institute of Technology Ladkrabang Research Fund [2566-02-01-036] and Thailand's National Science and Technology Development Agency (NSTDA) [JRA-CO-2565-17099-TH]. The authors used Google Gemini to assist with language editing and improving clarity of the manuscript. The scientific content and conclusions remain entirely the responsibility of the authors.

■ REFERENCES

(1) Nimsamer, P.; Mayuramart, O.; Rattanaburi, S.; Chantaravisoot, N.; Saengchoowong, S.; Puenpa, J.; Poovorawan, Y.; Payungporn, S. Comparative Performance of CRISPR-Cas12a Assays for SARS-CoV-2 Detection Tested with RNA Extracted from Clinical Specimens. *J. Virol. Methods* **2021**, *290*, No. 114092.

(2) Zhou, Z.; Cho, I. H.; Kadam, U. S. CRISPR-Cas-Based Diagnostics in Biomedicine: Principles, Applications, and Future Trajectories. *Biosensors* **2025**, *15* (10), No. 660.

(3) Samacoits, A.; Nimsamer, P.; Mayuramart, O.; Chantaravisoot, N.; Sitthi-amorn, P.; Nakhakes, C.; Luangkamchorn, L.; Tongcham, P.; Zahm, U.; Suphanpayak, S.; Padungwattanachoke, N.; Leelarthaphin, N.; Huayhongthong, H.; Pisitkun, T.; Payungporn, S.; Hannanta-anan, P. Machine Learning-Driven and Smartphone-Based Fluorescence Detection for CRISPR Diagnostic of SARS-CoV-2. *ACS Omega* **2021**, *6* (4), 2727−2733.

(4) Chen, J.; Ma, E.; Harrington, L.; Tian, X.; Doudna, J. CRISPR-Cas12a Target Binding Unleashes Single-Stranded DNase Activity. *Science* **2018**, *360*, 436−439.

(5) Broughton, J. P.; Deng, X.; Yu, G.; Fasching, C. L.; Servellita, V.; Singh, J.; Miao, X.; Streithorst, J. A.; Granados, A.; Sotomayor-Gonzalez, A.; Zorn, K.; Gopez, A.; Hsu, E.; Gu, W.; Miller, S.; Pan, C. Y.; Guevara, H.; Wadford, D. A.; Chen, J. S.; Chiu, C. Y. CRISPR−Cas12-Based Detection of SARS-CoV-2. *Nat. Biotechnol.* **2020**, *38* (7), 870−874.

(6) Shen, J.; Chen, Z.; Xie, R.; Li, J.; Liu, C.; He, Y.; Ma, X.; Yang, H.; Xie, Z. CRISPR/Cas12a-Assisted Isothermal Amplification for Rapid and Specific Diagnosis of Respiratory Virus on an Microfluidic Platform. *Biosens. Bioelectron.* **2023**, *237*, No. 115523.

(7) Xie, Y.; Li, H.; Chen, F.; Udayakumar, S.; Arora, K.; Chen, H.; Lan, Y.; Hu, Q.; Zhou, X.; Guo, X.; Xiu, L.; Yin, K. Clustered Regularly Interspaced Short Palindromic Repeats-Based Microfluidic System in Infectious Diseases Diagnosis: Current Status, Challenges, and Perspectives. *Adv. Sci.* **2022**, *9* (34), No. 2204172, DOI: 10.1002/advs.202204172.

(8) Nunes, J. K.; Stone, H. A. Introduction: Microfluidics. *Chem. Rev.* **2022**, *122*, 6919−6920, DOI: 10.1021/acs.chemrev.2c00052.

(9) Pol, R.; Céspedes, F.; Gabriel, D.; Baeza, M. Microfluidic Lab-on-a-Chip Platforms for Environmental Monitoring. *TrAC, Trends Anal. Chem.* **2017**, *95*, 62−68.

(10) Huang, D.; Ni, D. S.; Fang, M.; Shi, Z.; Xu, Z. Microfluidic Ruler-Readout and CRISPR Cas12a-Responded Hydrogel-Integrated Paper-Based Analytical Devices (MReaCH-PAD) for Visible Quantitative Point-of-Care Testing of Invasive Fungi. *Anal. Chem.* **2021**, *93* (50), 16965−16973.

(11) Cao, H.; Mao, K.; Ran, F.; Xu, P.; Zhao, Y.; Zhang, X.; Zhou, H.; Yang, Z.; Zhang, H.; Jiang, G. Paper Device Combining CRISPR/Cas12a and Reverse-Transcription Loop-Mediated Isothermal Amplification for SARS-CoV-2 Detection in Wastewater. *Environ. Sci. Technol.* **2022**, *56* (18), 13245−13253.

(12) English, M. A.; Soenksen, L. R.; Gayet, R. V.; de Puig, H.; Angenent-Mari, N. M.; Mao, A. S.; Nguyen, P. Q.; Collins, J. J. Programmable CRISPR-Responsive Smart Materials. *Science* **2019**, *365* (6455), 780−785.

(13) Yin, K.; Ding, X.; Li, Z.; Sfeir, M. M.; Ballesteros, E.; Liu, C. Autonomous Lab-on-Paper for Multiplexed, CRISPR-Based Diagnostics of SARS-CoV-2. *Lab Chip* **2021**, *21* (14), 2730−2737.

(14) Sen, A.; Morris, C.; Priye, A.; Broom, M. A Paper Based Microfluidic Platform Combining LAMP-CRISPR/Cas12a for Fluorometric Detection of Nucleic Acids *bioRxiv* 2023 DOI: 10.1101/2023.03.02.530841.

(15) Ruiz, R. A.; Gonzalez, J. L.; Vazquez-Alvarado, M.; Martinez, N. W.; Martinez, A. W. Beyond Wax Printing: Fabrication of Paper-Based Microfluidic Devices Using a Thermal Transfer Printer. *Anal. Chem.* **2022**, *94* (25), 8833−8837.

(16) Cai, J.; Jin, T.; Kou, J.; Zou, S.; Xiao, J.; Meng, Q. Lucas-Washburn Equation-Based Modeling of Capillary-Driven Flow in Porous Systems. *Langmuir* **2021**, *37* (5), 1623−1636.

(17) Liu, Z.; Hu, J.; Zhao, Y.; Qu, Z.; Xu, F. Experimental and Numerical Studies on Liquid Wicking into Filter Papers for Paper-Based Diagnostics. *Appl. Therm. Eng.* **2015**, *88*, 280−287.

(18) Hong, S.; Kim, W. Dynamics of Water Imbibition through Paper Channels with Wax Boundaries. *Microfluid. Nanofluidics* **2015**, *19* (4), 845−853.

(19) Compiro, P.; Chomta, N.; Nimnual, J.; Sunantawanit, S.; Payungporn, S.; Rotcheewaphan, S.; Keawsapsak, P. CRISPR-Cas12a-Based Detection and Differentiation of Mycobacterium Spp. *Clin. Chim. Acta* **2025**, *567*, No. 120101.

(20) Lim, H.; Jafry, A. T.; Lee, J. Fabrication, Flow Control, and Applications of Microfluidic Paper-Based Analytical Devices. *Molecules* **2019**, *24* (16), No. 2869.

(21) Li, W.; Ma, X.; Yong, Y. C.; Liu, G.; Yang, Z. Review of Paper-Based Microfluidic Analytical Devices for in-Field Testing of Pathogens. *Anal. Chim. Acta* **2023**, *1278*, No. 341614.

(22) Carrilho, E.; Martinez, A. W.; Whitesides, G. M. Understanding Wax Printing: A Simple Micropatterning Process for Paper-Based Microfluidics. *Anal. Chem.* **2009**, *81* (16), 7091−7095.

(23) Noviana, E.; Ozer, T.; Carrell, C. S.; Link, J. S.; McMahon, C.; Jang, I.; Henry, C. S. Microfluidic Paper-Based Analytical Devices: From Design to Applications. *Chem. Rev.* **2021**, *121* (19), 11835−11885.

(24) Ng, J. S.; Hashimoto, M. Fabrication of Paper Microfluidic Devices Using a Toner Laser Printer. *RSC Adv.* **2020**, *10* (50), 29797−29807.

(25) Ghosh, R.; Gopalakrishnan, S.; Savitha, R.; Renganathan, T.; Pushpavanam, S. Fabrication of Laser Printed Microfluidic Paper-Based Analytical Devices (LP-MPADs) for Point-of-Care Applications. *Sci. Rep.* **2019**, *9* (1), No. 7896, DOI: 10.1038/s41598-019-44455-1.
(26) Lin, Y. C.; Cho, J.; Tompsett, G. A.; Westmoreland, P. R.; Huber, G. W. Kinetics and Mechanism of Cellulose Pyrolysis. *J. Phys. Chem. C* **2009**, *113* (46), 20097−20107.
(27) Monju, T.; Hirakawa, M.; Kuboyama, S.; Saiki, R.; Ishida, A. A Fabrication Technique for Paper-Based Analytical Devices via Two-Sided Patterning with Thermal-Transfer Printer and Laminator. *Sens. Actuators, B* **2023**, *375*, No. 132886.
(28) Zhang, K.; Fan, Z.; Yao, B.; Ding, Y.; Zhao, J.; Xie, M.; Pan, J. Exploring the Trans-Cleavage Activity of CRISPR-Cas12a for the Development of a Mxene Based Electrochemiluminescence Biosensor for the Detection of Siglec-5. *Biosens. Bioelectron.* **2021**, *178*, No. 113019.
(29) Bandopadhyay, A.; Das, P. K. Paper Based Microfluidic Devices: A Review of Fabrication Techniques and Applications. *Eur. Phys. J.:Spec. Top.* **2023**, *232* (6), 781−815.
(30) Zhang, A.; Li, Y. Thermal Conductivity of Aluminum Alloys—A Review. *Materials* **2023**, *16* (8), No. 2972.
(31) Luo, X.; Feng, H.; Liu, J.; Liu, M. L.; Liu, S. In *An Experimental Investigation on Thermal Contact Resistance across Metal Contact Interfaces*; ICEPT-HDP 2011 Proceedings - 2011 International Conference on Electronic Packaging Technology and High Density Packaging; IEEE, 2011; pp 733−738 .
(32) Kim, D.; Nam, J.; Lee, B. J. Plasmon Thermal Conductivity of Thin Au and Ag Films. *Phys. Rev. B* **2023**, *108*, No. 205418, DOI: 10.1103/PhysRevB.108.205418.
(33) Ferreira, M.; Carvalho, V.; Ribeiro, J.; Lima, R. A.; Teixeira, S.; Pinho, D. Advances in Microfluidic Systems and Numerical Modeling in Biomedical Applications: A Review. *Micromachines* **2024**, *15* (7), No. 873.
(34) Martinez, A. W.; Phillips, S. T.; Whitesides, G. M.; Carrilho, E. Diagnostics for the Developing World: Microfluidic Paper-Based Analytical Devices. *Anal. Chem.* **2010**, *82* (1), 3−10.
(35) Yetisen, A. K.; Akram, M. S.; Lowe, C. R. Paper-Based Microfluidic Point-of-Care Diagnostic Devices. *Lab Chip* **2013**, *13* (12), 2210−2251.
(36) Cate, D. M.; Adkins, J. A.; Mettakoonpitak, J.; Henry, C. S. Recent Developments in Paper-Based Microfluidic Devices. *Anal. Chem.* **2015**, *87* (1), 19−41.
(37) Liu, Q.; Liu, M.; Jin, Y.; Li, B. Ratiometric Fluorescent Probe: A Sensitive and Reliable Reporter for the CRISPR/Cas12a-Based Biosensing Platform. *Analyst* **2022**, *147* (11), 2567−2574.
(38) Liu, S.; Xie, T.; Huang, Z.; Pei, X.; Li, S.; He, Y.; Tong, Y.; Liu, G. Systematically Investigating the Fluorescent Signal Readout of CRISPR-Cas12a for Highly Sensitive SARS-CoV-2 Detection. *Sens. Actuators, B* **2022**, *373*, No. 132746.
(39) Shah, K. G.; Yager, P. Wavelengths and Lifetimes of Paper Autofluorescence: A Simple Substrate Screening Process to Enhance the Sensitivity of Fluorescence-Based Assays in Paper. *Anal. Chem.* **2017**, *89* (22), 12023−12029.
(40) Lee, S.; Nam, D.; Park, J. S.; Kim, S.; Lee, E. S.; Cha, B. S.; Park, K. S. Highly Efficient DNA Reporter for CRISPR/Cas12a-Based Specific and Sensitive Biosensor. *Biochip J.* **2022**, *16* (4), 463−470.
(41) Zhang, J.; Guan, X.; Moon, J.; Zhang, S.; Jia, Z.; Yang, R.; Hou, C.; Guo, C.; Pei, M.; Liu, C. Interpreting CRISPR-Cas12a Enzyme Kinetics through Free Energy Change of Nucleic Acids. *Nucleic Acids Res.* **2024**, *52* (22), 14077−14092.
(42) Lightfield, J.; Fram, N. R.; Ely, B. Across Bacterial Phyla, Distantly-Related Genomes with Similar Genomic GC Content Have Similar Patterns of Amino Acid Usage. *PLoS One* **2011**, *6* (3), No. e17677.
(43) Tanifuji, Y.; Suzuki, H.; Tong, G.; Hiruta, Y.; Citterio, D. Basic Evaluation of the CRISPR/Cas System Stability for Application to Paper-Based Analytical Devices. *Anal. Methods* **2024**, *16* (25), 4143−4149.
(44) Hao, X.; Lou, H.; Bai, J.; Ding, Y.; Yang, J.; Pan, W. Cost-Effectiveness Analysis of Xpert in Detecting Mycobacterium Tuberculosis: A Systematic Review. *Int. J. Infect. Dis.* **2020**, *95*, 98−105.
(45) Lee, D. J.; Kumarasamy, N.; Resch, S. C.; Sivaramakrishnan, G. N.; Mayer, K. H.; Tripathy, S.; Paltiel, A. D.; Freedberg, K. A.; Reddy, K. P. Rapid, Point-of-Care Diagnosis of Tuberculosis with Novel Truenat Assay: Cost-Effectiveness Analysis for India's Public Sector. *PLoS One* **2019**, *14* (7), No. e0218890.
(46) Youngquist, B. M.; Saliba, J.; Kim, Y.; Cutro, T. J.; Lyon, C. J.; Olivo, J.; Ha, N.; Fine, J.; Colman, R.; Vergara, C.; Robinson, J.; LaCourse, S.; Garfein, R. S.; Catanzaro, D. G.; Lange, C.; Perez-Then, E.; Graviss, E. A.; Mitchell, C. D.; Rodwell, T.; Ning, B.; Hu, T. Y. Rapid Tuberculosis Diagnosis from Respiratory or Blood Samples by a Low Cost, Portable Lab-in-Tube Assay. *Sci. Transl. Med.* **2025**, *17*, No. eadp6411, DOI: 10.1126/scitranslmed.adp6411.
(47) Hernandez-Garcia, A.; Morales-Moreno, M. D.; Valdés-Galindo, E. G.; Jimenez-Nieto, E. P.; Quezada, A. Diagnostics of COVID-19 Based on CRISPR−Cas Coupled to Isothermal Amplification: A Comparative Analysis and Update. *Diagnostics* **2022**, *12* (6), No. 1434.
(48) Bell, A. G.; Dunkley, O. R. S.; Modi, N. H.; Huang, Y.; Tseng, S.; Reiss, R.; Daivaa, N.; Davis, J. L.; Vargas, D. A.; Banada, P.; Xie, Y. L.; Myhrvold, C. A Streamlined CRISPR-Based Test for Tuberculosis Detection Directly from Sputum. *Sci. Adv.* **2025**, *11* (32), No. 2067.
(49) Myhrvold, C.; Freije, C. A.; Gootenberg, J. S.; Abudayyeh, O. O.; Metsky, H. C.; Durbin, A. F.; Kellner, M. J.; Tan, A. L.; Paul, L. M.; Parham, L. A.; Garcia, K. F.; Barnes, K. G.; Chak, B.; Mondini, A.; Nogueira, M. L.; Isern, S.; Michael, S. F.; Lorenzana, I.; Yozwiak, N. L.; MacInnis, B. L.; Bosch, I.; Gehrke, L.; Zhang, F.; Sabeti, P. C. Field-Deployable Viral Diagnostics Using CRISPR-Cas13. *Science* **2018**, *360* (6387), 444−448.
(50) Kaminski, M. M.; Abudayyeh, O. O.; Gootenberg, J. S.; Zhang, F.; Collins, J. J. CRISPR-Based Diagnostics. *Nat. Biomed. Eng.* **2021**, *5* (7), 643−656.
(51) Ding, X.; Yin, K.; Li, Z.; Lalla, R. V.; Ballesteros, E.; Sfeir, M. M.; Liu, C. Ultrasensitive and Visual Detection of SARS-CoV-2 Using All-in-One Dual CRISPR-Cas12a Assay. *Nat. Commun.* **2020**, *11* (1), No. 4711.
(52) Joung, J.; Ladha, A.; Saito, M.; Kim, N.-G.; Woolley, A. E.; Segel, M.; Barretto, R. P. J.; Ranu, A.; Macrae, R. K.; Faure, G.; Ioannidi, E. I.; Krajeski, R. N.; Bruneau, R.; Huang, M.-L. W.; Yu, X. G.; Li, J. Z.; Walker, B. D.; Hung, D. T.; Greninger, A. L.; Jerome, K. R.; Gootenberg, J. S.; Abudayyeh, O. O.; Zhang, F. Detection of SARS-CoV-2 with SHERLOCK One-Pot Testing. *N. Engl. J. Med.* **2020**, *383* (15), 1492−1494.
(53) Lim, J.; Van, A. B.; Koprowski, K.; Wester, M.; Valera, E.; Bashir, R. Amplification-Free, OR-Gated CRISPR-Cascade Reaction for Pathogen Detection in Blood Samples. *Proc. Natl. Acad. Sci. U.S.A.* **2025**, *122* (11), No. e2420166122, DOI: 10.1073/pnas.2420166122.
(54) Jang, H.; Kang, J. E.; Kim, H.; Kim, J. R.; Park, J.; Go, S. R.; Lee, Y. H.; Kang, H.; Park, Y.; Kim, S.; Jung, Y.; Kim, S. J.; Lim, E. K.; Jung, J.; Woo, E. J.; Park, K. H.; Kang, T. CRISPR/Cas12a2 Enables Ultra-Sensitive Amplification-Free RNA Detection. *Nucleic Acids Res.* **2025**, *53* (21), No. gkaf1293, DOI: 10.1093/nar/gkaf1293.

https://doi.org/10.1021/acsomega.6c00845
ACS Omega 2026, 11, 31169−31181